Increasing Solar Absorption for Photocatalysis with Black Hydrogenated Titanium Dioxide Nanocrystals

Xiaobo Chen, *et al.*

Science **331**, 746 (2011);
DOI: 10.1126/science.1200448

20. R. H. Baughman, S. Stafström, C. Cui, S. O. Dantas, *Science* **279**, 1522 (1998).
21. U. Mitzdorf, D. Helmreich, *J. Acoust. Soc. Am.* **49**, 723 (1971).
22. G. V. Yukhnevich, E. G. Tarakanova, *J. Mol. Struct.* **447**, 257 (1998).
23. R. Lakes, K. W. Wojciechowski, *Physica Stat. Solidi B* **245**, 545 (2008).
24. J. N. Grima, D. Attard, R. Gatt, *Physica Stat. Solidi B* **245**, 2405 (2008).
25. A. L. Goodwin, *Z. Krist.* **1** (suppl. 30), 1 (2009).

26. We thank I. Wood for useful discussions; the Institut Laue Langevin and the ISIS facility for beam time; and J.-L. Laborier, C. Payre, and L. Gendrin for invaluable technical assistance in carrying out the high-pressure measurements at the ILL. This work was funded under fellowships from STFC (ex Particle Physics and Astronomy Research Council, PPARC) grant nos. PPA/P/S/2003/00247 and PP/E006515/1.

Supporting Online Material
www.sciencemag.org/cgi/content/full/331/6018/742/DC1
Materials and Methods
Figs. S1 to S14
Tables S1 to S18
References

4 October 2010; accepted 5 January 2011
10.1126/science.1198640

Increasing Solar Absorption for Photocatalysis with Black Hydrogenated Titanium Dioxide Nanocrystals

Xiaobo Chen,[1,2] Lei Liu,[1,3] Peter Y. Yu,[1,3] Samuel S. Mao[1,2]*

When used as a photocatalyst, titanium dioxide (TiO_2) absorbs only ultraviolet light, and several approaches, including the use of dopants such as nitrogen, have been taken to narrow the band gap of TiO_2. We demonstrated a conceptually different approach to enhancing solar absorption by introducing disorder in the surface layers of nanophase TiO_2 through hydrogenation. We showed that disorder-engineered TiO_2 nanocrystals exhibit substantial solar-driven photocatalytic activities, including the photo-oxidation of organic molecules in water and the production of hydrogen with the use of a sacrificial reagent.

The effectiveness of solar-driven photocatalytic processes underlying hydrogen production and water decontamination is dictated to a great extent by the semiconductor's capability of absorbing visible and infrared light, as well as its ability to suppress the rapid combination of photogenerated electrons and holes. Nanophase titanium dioxide (TiO_2), which has a large surface area that can facilitate a fast rate of surface reactions, is a widely used wide–band-gap semiconductor photocatalyst for a variety of solar-driven clean energy and environmental technologies (*1*–*4*). In order to increase the limited optical absorption of TiO_2 under sunlight, there have been persistent efforts to vary the chemical composition of TiO_2 by adding controlled metal (*5*, *6*) or nonmetal (*7*–*10*) impurities that generate donor or acceptor states in the band gap. Different from impurity incorporation, self-doping that produces Ti^{3+} species in TiO_2 has also been demonstrated (*11*). Through doping, the solar absorption characteristics of TiO_2 have been improved to some extent. For example, when nonmetallic light-element dopants are introduced (*9*), the optical absorption of TiO_2 can be modified as the result of electronic transitions from the dopant 2*p* or 3*p* orbitals to the Ti 3*d* orbitals. At present, nitrogen-doped TiO_2 exhibits the greatest optical response to solar radiation (*3*), but its absorption in the visible and infrared remains insufficient.

We developed an alternative approach to improving visible and infrared optical absorption by engineering the disorder of nanophase TiO_2 with simultaneous dopant incorporation. In its simplest form, a disorder-engineered nanophase TiO_2 consists of two phases: a crystalline TiO_2 quantum dot or nanocrystal as a core, and a highly disordered surface layer where dopants are introduced (Fig. 1A). Although an ensemble of

[1]Lawrence Berkeley National Laboratory, University of California at Berkeley, Berkeley, CA 94720, USA. [2]Department of Mechanical Engineering, University of California at Berkeley, Berkeley, CA 94720, USA. [3]Department of Physics, University of California at Berkeley, Berkeley, CA 94720, USA.

*To whom correspondence should be addressed. E-mail: ssmao@lbl.gov

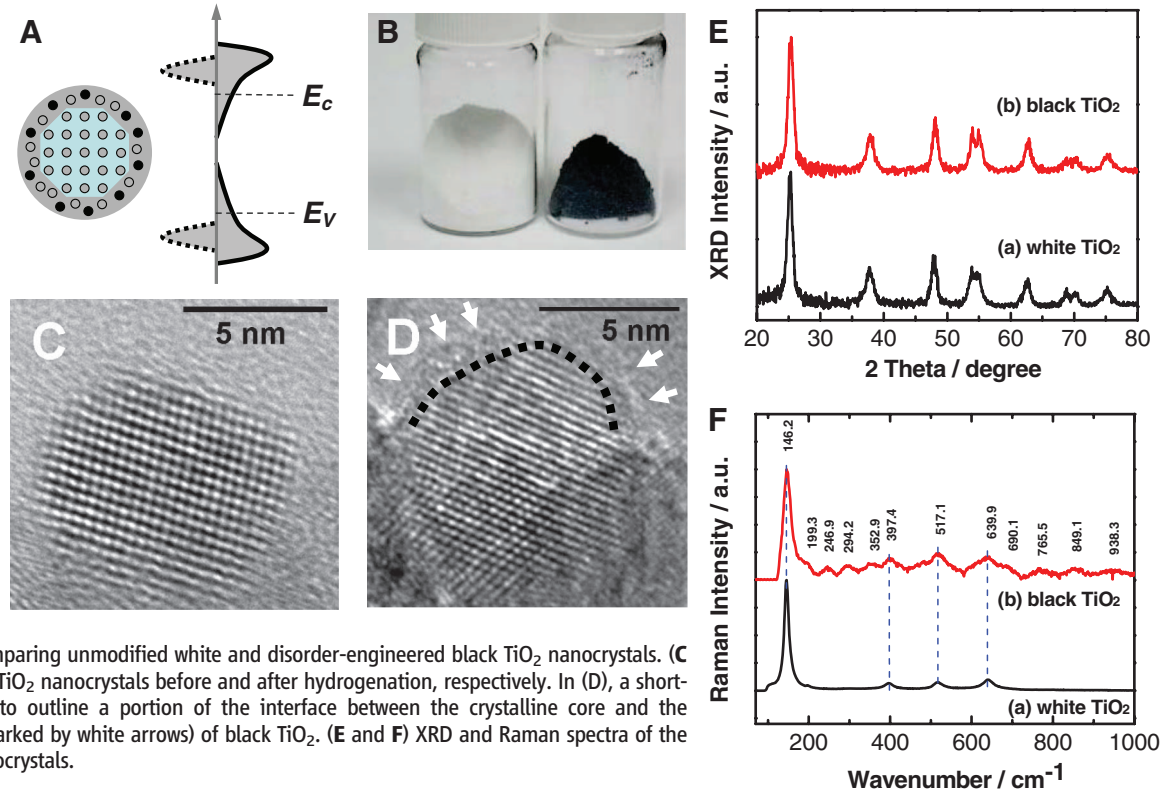

Fig. 1. (**A**) Schematic illustration of the structure and electronic DOS of a semiconductor in the form of a disorder-engineered nanocrystal with dopant incorporation. Dopants are depicted as black dots, and disorder is represented in the outer layer of the nanocrystal. The conduction and valence levels of a bulk semiconductor, E_C and E_V, respectively, are also shown, and the bands of the nanocrystals are shown at the left. The effect of disorder, which creases broadened tails of states extending into the otherwise forbidden band gap, is shown at the right. (**B**) A photo comparing unmodified white and disorder-engineered black TiO_2 nanocrystals. (**C** and **D**) HRTEM images of TiO_2 nanocrystals before and after hydrogenation, respectively. In (D), a short-dashed curve is applied to outline a portion of the interface between the crystalline core and the disordered outer layer (marked by white arrows) of black TiO_2. (**E** and **F**) XRD and Raman spectra of the white and black TiO_2 nanocrystals.

nanocrystals retains the benefits of crystalline TiO_2 quantum structures for photocatalytic processes, the introduction of disorder and dopant at their surface would enhance visible and infrared absorption, with the additional benefit of carrier trapping. Large amounts of lattice disorder in semiconductors could yield mid-gap states whose energy distributions differ from that of a single defect in a crystal. For example, instead of forming discrete donor states near the conduction band edge, these mid-gap states can form a continuum extending to and overlapping with the conduction band edge; thus they are often also known as band tail states. Similarly large amounts of disorder can result in band tail states merging with the valence band (*12*–*15*). These extended energy states, in combination with the energy levels produced by dopants, can become the dominant centers for optical excitation and relaxation. An additional potential advantage of these engineered disorders is that they provide trapping sites for photogenerated carriers and prevent them from rapid recombination, thus promoting electron transfer and photocatalytic reactions. The density of states (DOS) of disorder-engineered semiconductor nanocrystals, as compared to those of unmodified nanocrystals, is shown schematically in Fig. 1A.

To introduce disorders into nanophase TiO_2 with simultaneous dopant addition, we generated a porous network of TiO_2 nanocrystals, a few nanometers in diameter. Hydrogenation of this material creates a disordered layer on the nanocrystal surface. We observed a shift in the onset of absorption in such disorder-engineered TiO_2 nanocrystals, from the ultraviolet (UV) to near-infrared after hydrogenation, accompanied by a dramatic color change and substantial enhancement of solar-driven photocatalytic activity. A photo of disorder-engineered black TiO_2 nanocrystals, as compared to one of unmodified white TiO_2 nanocrystals, is shown in Fig. 1B.

We prepared TiO_2 nanocrystals with a precursor solution consisting of titanium tetraisopropoxide (TTIP), ethanol, hydrochloric acid (HCl), deionized water, and an organic template, Pluronic F127, with molar ratios of TTIP/F127/HCl/H_2O/ethanol at 1:0.005:0.5:15:40. The solution was heated at 40°C for 24 hours and then evaporated and dried at 110°C for 24 hours. The dried powders were calcinated at 500°C for 6 hours to remove the organic template and enhance the crystallization of TiO_2. Both the temperature ramp rate and the cooling rate were approximately 0.3°C min^{-1}. The resulting white-colored powders were first maintained in a vacuum for 1 hour after being placed in the sample chamber of a Hy-Energy PCTPro high-pressure hydrogen system and then hydrogenated in a 20.0-bar H_2 atmosphere at about 200°C for 5 days. Because hydrogen tends to be attracted to dangling bonds, we expected the concentration of hydrogen to be the highest in the disordered layer, where there are substantially more dangling bonds than in the crystalline core of black TiO_2 nanoparticles.

We investigated the structures of the TiO_2 nanocrystals before and after hydrogenation with x-ray diffraction (XRD), Raman spectroscopy, and scanning and transmission electron microscopy (SEM and TEM). The pure TiO_2 nanocrystals were highly crystallized, as seen from the well-resolved lattice features shown in the high-resolution TEM (HRTEM) image (Fig. 1C); the size of individual TiO_2 nanocrystals was approximately 8 nm in diameter. After hydrogenation, however, the surfaces of TiO_2 nanocrystals became disordered (Fig. 1D) where the disordered outer layer surrounding a crystalline core was ~1 nm in thickness. Strong XRD diffraction peaks (Fig. 1E) also indicate that the TiO_2 nanocrystals were highly crystallized. The crystalline phase had an anatase structure with an average crystal size of approximately 8 nm, in agreement with HRTEM observation.

We used Raman spectroscopy to examine structural changes in the TiO_2 nanocrystals after the introduction of disorder with hydrogenation. The three polymorphs of TiO_2 belong to different space groups: $D_{4h}^{19}(I4_1/amd)$ for anatase, D_{2h}^{15} (*pbca*) for brookite, and $D_{4h}^{14}(P4_2/mnm)$ for rutile, which have distinctive characteristics in Raman spectra. For anatase TiO_2, there are six Raman-active modes with frequencies at 144, 197, 399, 515, 519 (superimposed with the 515 cm^{-1} band), and 639 cm^{-1}, respectively (*3*). The unmodified white TiO_2 nanocrystals display the typical anatase Raman bands, but new bands at 246.9, 294.2, 352.9, 690.1, 765.5, 849.1, and 938.3 cm^{-1} emerge for the black TiO_2 nanocrystals, in addition to the broadening of the anatase Raman peaks (Fig. 1F). These Raman bands cannot be assigned to any of the three polymorphs of TiO_2, which indicates that structural changes occur after hydrogenation, resulting in disorders that can activate zone-edge and otherwise Raman-forbidden modes (such as modes that are infrared-active only) by breaking down the Raman selection rule (*13*).

The solar-driven photocatalytic activity of the disorder-engineered black TiO_2 nanocrystals was measured by monitoring the change in optical absorption of a methylene blue solution at ~660 nm during its photocatalytic decomposition process. Other than being a nitrogenous reference compound for evaluating photocatalysts, methylene blue can be found as a water contaminant from dyeing processes. In a typical experiment, 0.15 mg of black TiO_2 nanocrystals was added to a 3.0-ml methylene blue solution that had an optical density (OD) of approximately 1.0 under aerobic conditions; the results were corrected for methylene

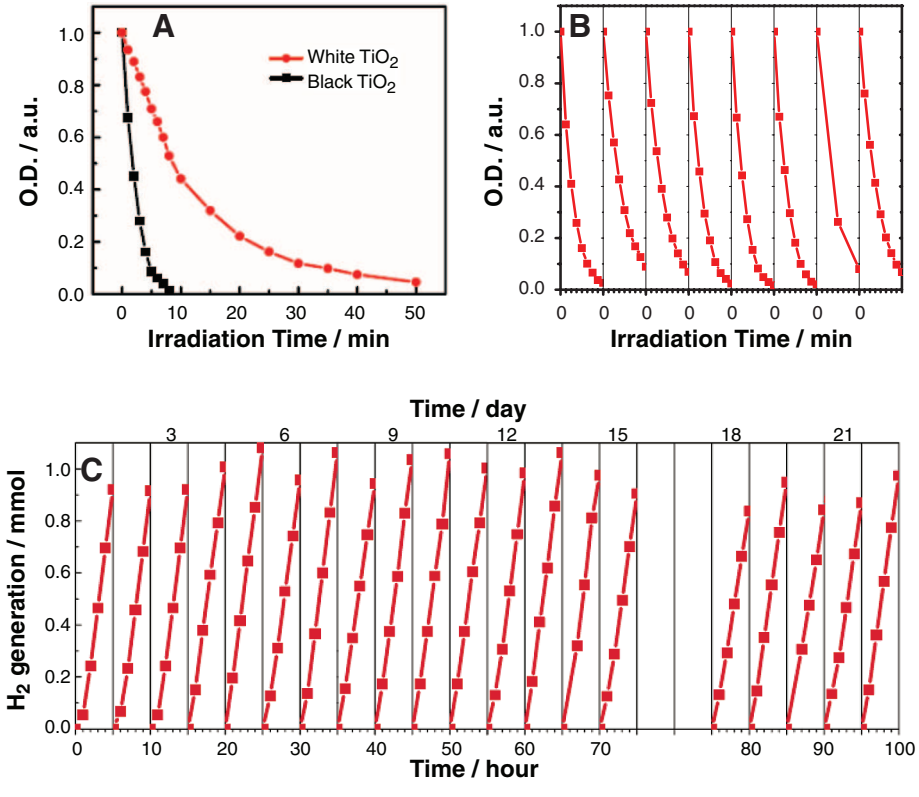

Fig. 2. (**A**) Comparison of the solar-driven photocatalytic activity of the black TiO_2 nanocrystals with that of the white TiO_2 nanocrystals under the same experimental conditions. The *y* axis represents the optical density of the methylene blue solution, whereas the *x* axis is the solar light irradiation time. a.u., arbitrary units. (**B**) Cycling tests of solar-driven photocatalytic activity (methylene blue decomposition) of the disorder-engineered black TiO_2 nanocrystals. Data in the figure represent the first 8 min of measurements in each of the eight consecutive photodegradation testing cycles. (**C**) Cycling measurements of hydrogen gas generation through direct photocatalytic water splitting with disorder-engineered black TiO_2 nanocrystals under simulated solar light. Experiments were conducted in a 22-day period, with 100 hours of overall solar irradiation time.

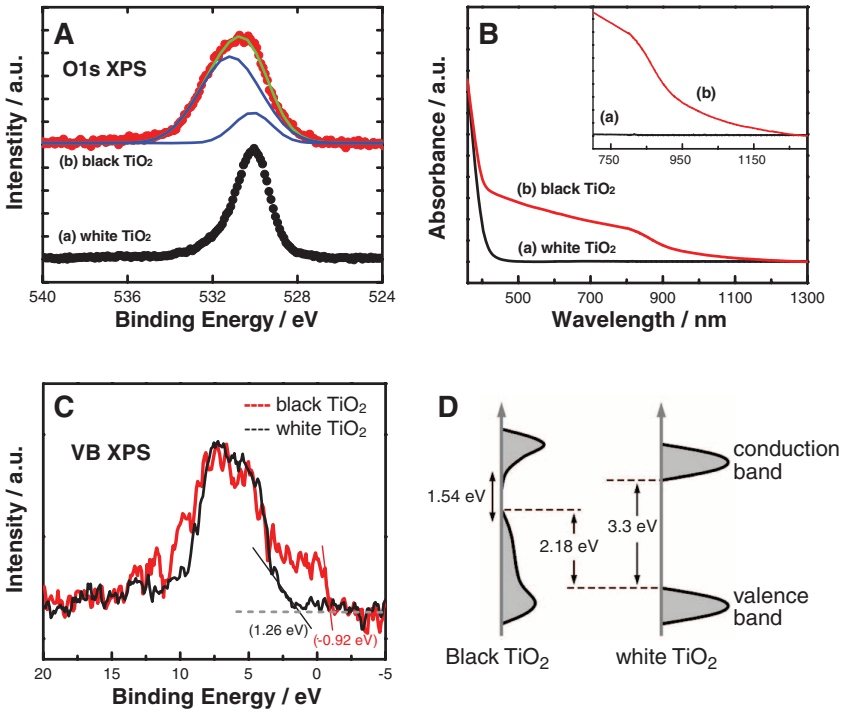

Fig. 3. (**A**) O 1*s* XPS spectra of the white and black TiO_2 nanocrystals. The red and black circles are XPS data. The green curve is the fitting of experimental data for black TiO_2 nanocrystals, which can be decomposed into a superposition of two peaks shown as blue curves. (**B**) Spectral absorbance of the white and black TiO_2 nanocrystals. The inset enlarges the absorption spectrum in the range from approximately 750 to 1200 nm. (**C**) Valence-band XPS spectra of the white and black TiO_2 nanocrystals. (**D**) Schematic illustration of the DOS of disorder-engineered black TiO_2 nanocrystals, as compared to that of unmodified TiO_2 nanocrystals.

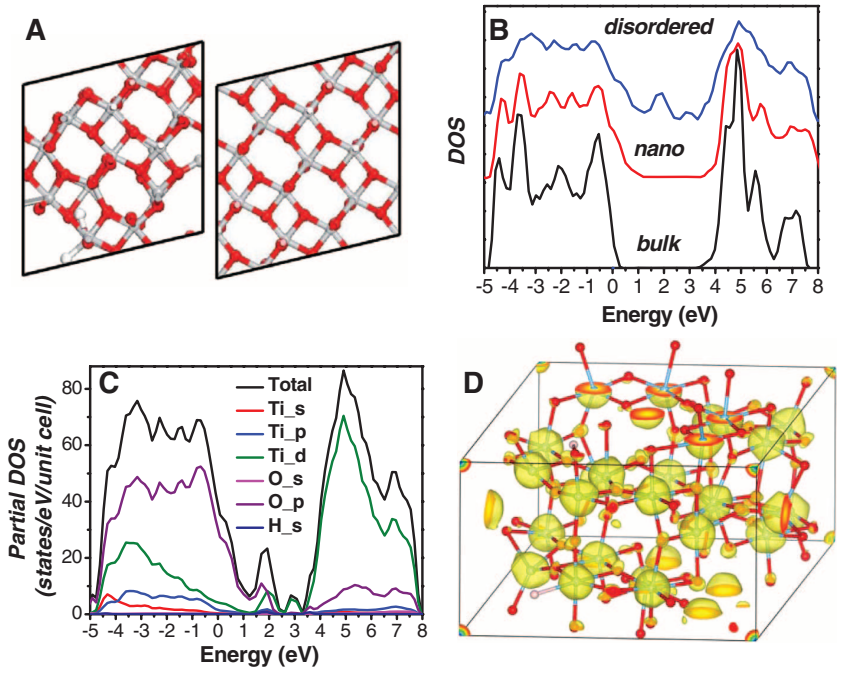

Fig. 4. (**A**) Schematic illustration of a supercell for modeling a disorder-engineered TiO_2 nanocrystal (red, O atoms; gray, Ti atoms; white, H atoms), as compared to a supercell modeling bulk anatase TiO_2. (**B**) Calculated DOS of TiO_2 in the form of a disorder-engineered nanocrystal, an unmodified nanocrystal, and a bulk crystal. The energy of the valence band maximum of the bulk phase is taken to be zero. (**C**) Decomposition of the total DOS of disorder-engineered black TiO_2 nanocrystals into partial DOS of the Ti, O, and H orbitals. (**D**) Three-dimensional plot of calculated charge density distribution of a mid-gap electronic state (at about 1.8 eV) of disorder-engineered TiO_2 nanocrystals.

blue degradation in the absence of any photocatalyst [see the supporting online material (SOM) and fig. S1]. Photodegration was complete after 8 min for the black TiO_2 nanocrystals, whereas for the unmodified white TiO_2 nanocrystals under the same testing conditions, it took nearly 1 hour (Fig. 2A). Similar improvement was also observed for the photocatalytic decomposition of phenol (SOM and fig. S2).

The results of cycling tests of the solar-driven photocatalytic activity of black TiO_2 nanocrystals in decomposing methylene blue are shown in Fig. 2B. Once the photocatalytic reaction of a testing cycle was complete, the subsequent cycle was started after an amount of concentrated methylene blue compound was added to make the OD of the solution approximately 1.0. The disorder-engineered black TiO_2 nanocrystals did not exhibit any reduction of their photocatalytic activity under solar irradiation after eight photocatalysis cycles.

The disorder-engineered black TiO_2 nanocrystals exhibit substantial activity and stability in the photocatalytic production of hydrogen from water under sunlight. Hydrogen gas evolution as a function of time during a 22-day testing period of solar hydrogen production experiments using black TiO_2 nanocrystals as the photocatalysts is shown in Fig. 2C. A full-spectrum solar simulator was used as the excitation source, which produced about 1 Sun power at the sample consisting of black TiO_2 nanocrystals loaded with 0.6 weight % Pt, placed in a Pyrex glass container filled with 1:1 water-methanol solution (methanol is the sacrificial reagent, and the anodic reaction generating O_2 from H_2O is not occurring in this system). Measurements were conducted initially for 15 consecutive days; each day the sample was irradiated for 5 hours and then stored in darkness overnight before testing the next day. We found that 1 hour of solar irradiation generated 0.2 ± 0.02 mmol of H_2 using 0.02 g of disorder-engineered black TiO_2 nanocrystals (10 mmol $hour^{-1}$ g^{-1} of photocatalysts). This H_2 production rate is about two orders of magnitude greater than the yields of most semiconductor photocatalysts (*2*, *16*). The energy conversion efficiency for solar hydrogen production, defined as the ratio between the energy of solar-produced hydrogen and the energy of the incident sunlight, reached 24% for disorder-engineered black TiO_2 nanocrystals.

After testing for 13 days, 30 ml of pure water was added to compensate for the loss, and measurements continued for 2 additional days before the sample was stored in darkness for 2 days (days 16 and 17) without measurements. Experiments were resumed for 5 more days after the 2-day storage period, and similar rates of H_2 evolution were still observed. Throughout the testing cycles, the disorder-engineered black TiO_2 nanocrystals exhibited persistent high H_2 production capability. Under the same experimental conditions, no H_2 gas was detected from the unmodified white TiO_2 nanocrystals loaded with

Pt. We performed experiments to quantify the amount of hydrogen absorbed in black TiO_2 photocatalysts (SOM and fig. S3). The 20.0 mg of black TiO_2 photocatalysts that were used to generate 40 mg of H_2 in 100 hours contained only about 0.05 mg of H_2. The black TiO_2 photocatalysts did not act as a hydrogen reservoir in these experiments.

We also measured photocatalytic H_2 production, using black TiO_2 as the photocatalyst with only visible and infrared light by filtering out incident light with wavelengths shorter than about 400 nm. The rate of H_2 production dropped to 0.1 ± 0.02 mmol $hour^{-1}$ g^{-1} of photocatalysts, reflecting the activity of the extended tail or mid-gap states of the thin disordered layer, which have a narrower band gap created by disordering. This reduced H_2 production rate was about the same as that measured under the full solar spectrum but without using any sacrificial reagent. We examined the change of surface chemical bonding of TiO_2 nanocrystals induced by hydrogenation with x-ray photoelectron spectroscopy (XPS) using a Physical Electronics PHI 5400 system. The Ti 2*p* XPS spectra were almost identical for both the white and black TiO_2 nanocrystals (SOM and figs. S4 and S5), which indicates that Ti atoms have a similar bonding environment after hydrogenation and do not resemble spectra of TiO_2 doped with carbon or other impurities (*3*, *7*–*10*). The O 1*s* XPS spectra of the white and black TiO_2 nanocrystals show dramatic differences (Fig. 3A); the single O 1*s* peak at 530.0 eV, typical for white TiO_2, can be resolved into two peaks at about 530.0 and 530.9 eV for the black TiO_2 nanocrystals. The broader peak at 530.9 eV can be attributed to Ti-OH species (*17*). Diffusive reflectance and absorbance spectroscopy (Fig. 3B) revealed that the band gap of the unmodified white TiO_2 nanocrystals was approximately 3.30 eV, slightly greater than that of bulk anatase TiO_2. The onset of optical absorption of the black hydrogenated TiO_2 nanocrystals was lowered to about 1.0 eV (~1200 nm). An abrupt change in both the reflectance and absorbance spectra at approximately 1.54 eV (806.8 nm) suggests that the optical gap of the black TiO_2 nanocrystals was substantially narrowed by intraband transitions. No color change was observed for the black TiO_2 nanocrystals over 1 year after they were synthesized.

The density of states (DOS) of the valence band of TiO_2 nanocrystals was also measured by valence band XPS (Fig. 3C). The white TiO_2 nanocrystals displayed typical valence band DOS characteristics of TiO_2, with the edge of the maximum energy at about 1.26 eV. Because the band gap of the white TiO_2 is 3.30 eV from the optical absorption spectrum, the conduction band minimum would occur at about –2.04 eV. For the black TiO_2 nanocrystals, the valence band maximum energy blue-shifts toward the vacuum level at approximately –0.92 eV. Combined with the results from optical measurements that suggest a much narrowed band gap, the conduction band DOS of the black TiO_2 nanocrystals would not have as substantial a change. Nevertheless, there may be conduction band tail states arising from disorder that extend below the conduction band minimum. Optical transitions from the blue-shifted valence band edge to these band tail states are presumably responsible for optical absorption onset around 1.0 eV in black TiO_2. A schematic illustration of the DOS of disorder-engineered black TiO_2 nanocrystals is shown in Fig. 3D.

To understand the origin of the change in the electronic and optical properties of black TiO_2 nanocrystals, we calculated the energy band structures using a first-principles density functional theory (DFT) (*18*–*20*). Existing models of modified TiO_2 are focused on point defects, which tend to produce shallow or deep energy levels near the conduction band minimum with typical Ti^{3+} state characteristics (*21*–*23*). We studied on-lattice disorders in TiO_2 nanocrystals in the presence of hydrogen and found that, rather than generating levels near the conduction band minimum, disorder-induced mid-gap states can upshift the valence band edge of TiO_2 nanocrystals.

We first constructed a network of TiO_2 nanocrystals without disorder but with fully relaxed surface dangling bonds. From the calculated total and projected DOS (SOM and fig. S6), we found that the primary effect of surface reconstruction in TiO_2 nanocrystals is to produce strong band tailing near the valence band edge. The valence and conduction states are derived mainly from the O *2p* orbitals and the Ti 3*d* orbitals, respectively. Without the introduction of disorder, we examined the band structures of TiO_2 nanocrystals containing four types of intrinsic defects with low formation energies: Ti vacancy (V_{Ti}), O vacancy (V_O), interstitial titanium (I_{Ti}), and interstitial oxygen (I_O); and three types of hydrogen impurities: interstitial H atom (I_H), interstitial H_2 molecule (I_{H2}), and H atom forming surface OH bonds with oxygen ($OH_{surface}$). The three native defects, V_{Ti}, V_O, and I_O, do not introduce mid-gap states, which agrees with previous calculations (*24*). Similarly, no mid-gap states were produced as the result of the defects associated with hydrogen impurities (*22*, *23*). Based on the established DFT (*21*), without disorder, the only defect that could yield a gap state in TiO_2 nanocrystals, about 0.5 eV below the conduction band minimum, is the interstitial Ti atom, I_{Ti}.

When we introduced lattice disorders in hydrogenated anatase TiO_2 nanocrystals, mid-gap electronic states were created, accompanied by a reduced band gap. The disordered TiO_2 nanocrystal model, in which one H atom is bonded to an O atom while another H atom is bonded to a Ti atom, yields electronic band structures consistent with the valence band XPS measurements. A schematic illustration of a supercell of the disordered TiO_2 nanocrystal model as compared to that of a bulk anatase TiO_2 crystal is shown in Fig. 4A, and Fig. 4B plots the calculated DOS of the disorder-engineered TiO_2 nanocrystals along with those of the bulk and the unmodified TiO_2 nanocrystals. Two groups of mid-gap states (centered at about 1.8 and 3.0 eV) can be observed in the DOS of the disordered TiO_2 nanocrystals, for which the Fermi level was found to locate slightly below 2.0 eV. The different nature of these two groups of mid-gap states is revealed by the calculated partial DOS (Fig. 4C). Whereas the higher-energy mid-gap states (~3.0 eV) are derived from the Ti 3*d* orbitals only, the lower-energy states (~1.8 eV) are hybridized from both O 2*p* orbitals and Ti 3*d* orbitals, and mainly from the valence band states as the result of disorders stabilized by hydrogen. The hydrogen 1*s* orbital coupling to the Ti atom does not make a substantial contribution to either state, which suggests that lattice disorder accounts for the mid-gap states; hydrogen may have stabilized the lattice disorders by passivating their dangling bonds. Because the lower-energy mid-gap states lie below the Fermi level, they can account for a large blue shift of the valence band edge.

We also examined the three-dimensional charge density distribution of the mid-gap electronic states (Fig. 4D) of disorder-engineered TiO_2 nanocrystals. Charges associated with the lower-energy mid-gap states distributed around every O or Ti atom are indicative of the overall impact of the disorder. Because the lower-energy mid-gap states are derived from hybridization of the O 2*p* orbital with the Ti 3*d* orbital, optical transition between these mid-gap states and the conduction band tail would produce charge transfer from the O 2*p* orbital to the Ti 3*d* orbital, similar to the transition from the valence to the conduction band of bulk TiO_2. The localization of both photoexcited electrons and holes prevents fast recombination and presumably is the reason why disorder-engineered black TiO_2 can more efficiently harvest the infrared photons for photocatalysis than what bulk anatase can do to the above–band-gap UV photons.

References and Notes

1. M. Grätzel, *Nature* **414**, 338 (2001).
2. X. Chen, S. Shen, L. Guo, S. S. Mao, *Chem. Rev.* **110**, 6503 (2010).
3. X. Chen, S. S. Mao, *Chem. Rev.* **107**, 2891 (2007).
4. A. Fujishima, X. Zhang, A. D. Tryk, *Surf. Sci. Rep.* **63**, 515 (2008).
5. M. R. Hoffmann, S. T. Martin, W. Choi, D. W. Bahnemann, *Chem. Rev.* **95**, 69 (1995).
6. W. Choi, A. Termin, M. R. Hoffmann, *Angew. Chem.* **106**, 1148 (1994).
7. R. Asahi, T. Morikawa, T. Ohwaki, K. Aoki, Y. Taga, *Science* **293**, 269 (2001).
8. S. U. M. Khan, M. Al-Shahry, W. B. Ingler Jr., *Science* **297**, 2243 (2002).
9. X. Chen, C. Burda, *J. Am. Chem. Soc.* **130**, 5018 (2008).
10. X. Chen, C. Burda, *J. Phys. Chem. B* **108**, 15446 (2004).
11. F. Zuo *et al.*, *J. Am. Chem. Soc.* **132**, 11856 (2010).
12. J. Tauc, A. Abraham, L. Pajasova, R. Grigorovici, A. Vancu, *Non-Crystalline Solids* (North-Holland, Amsterdam, 1965).
13. P. Y. Yu, M. Cardona, *Fundamentals of Semiconductors: Physics and Materials Properties* (Springer, Heidelberg, ed. 4, 2010).
14. U. Diebold, *Surf. Sci. Rep.* **48**, 53 (2003).
15. T. L. Thompson, J. T. Yates Jr., *Chem. Rev.* **106**, 4428 (2006).
16. A. Kudo, Y. Miseki, *Chem. Soc. Rev.* **38**, 253 (2009).
17. E. McCafferty, J. P. Wightman, *Surf. Interface Anal.* **26**, 549 (1998).

18. G. Kresse, J. Hafner, *Phys. Rev. B* **47**, 558 (1993).
19. G. Kresse, J. Hafner, *Phys. Rev. B* **48**, 13115 (1993).
20. G. Kresse, J. Furthmüller, *Comput. Mater. Sci.* **6**, 15 (1996).
21. C. Di Valentin, G. Pacchioni, A. Selloni, *J. Phys. Chem. C* **113**, 20543 (2009).
22. C. G. Van de Walle, *Phys. Rev. Lett.* **85**, 1012 (2000).
23. Ç. Kiliç, A. Zunger, *Appl. Phys. Lett.* **81**, 73 (2002).
24. S. Na-Phattalung *et al.*, *Phys. Rev. B* **73**, 125205 (2006).
25. We thank M. S. Dresselhaus for encouragement, M. T. Lee and S. H. Shen for their assistance, and R. Greif for discussions and critical reading of the manuscript. This research has been supported by the Office of Energy Efficiency and Renewable Energy of the U.S. Department of Energy. S.S.M. and X.C. also acknowledge support from the King Abdullah University of Science and Technology–University of California Academic Excellence Alliance. TEM work was performed at the National Center for Electron Microscopy, which is supported by the Office of Science, Office of Basic Energy Sciences of the U.S. Department of Energy.

Supporting Online Material
www.sciencemag.org/cgi/content/full/science.1200448/DC1
Methods
SOM Text
Figs. S1 to S6
References

15 November 2010; accepted 11 January 2011
Published online 20 January 2011;
10.1126/science.1200448

Complete Fourth Metatarsal and Arches in the Foot of *Australopithecus afarensis*

Carol V. Ward,[1]* William H. Kimbel,[2] Donald C. Johanson[2]

The transition to full-time terrestrial bipedality is a hallmark of human evolution. A key correlate of human bipedalism is the development of longitudinal and transverse arches of the foot that provide a rigid propulsive lever and critical shock absorption during striding bipedal gait. Evidence for arches in the earliest well-known *Australopithecus* species, *A. afarensis*, has long been debated. A complete fourth metatarsal of *A. afarensis* was recently discovered at Hadar, Ethiopia. It exhibits torsion of the head relative to the base, a direct correlate of a transverse arch in humans. The orientation of the proximal and distal ends of the bone reflects a longitudinal arch. Further, the deep, flat base and tarsal facets imply that its midfoot had no ape-like midtarsal break. These features show that the *A. afarensis* foot was functionally like that of modern humans and support the hypothesis that this species was a committed terrestrial biped.

Although *Australopithecus afarensis* was primarily a terrestrial biped, there continues to be debate over the nature of its bipedality and the extent to which its morphology represents a compromise between terrestrial bipedality and arboreal locomotion. One of the key adaptations to a human-like striding bipedal gait is the evolution of permanent transverse and longitudinal pedal arches (*1*, *2*). The arches, supported by bone and soft tissue, provide an important mechanism for shock absorption during the stance phase of gait (*3*) and a rigid lever at heel-off, as well as permit flexibility during locomotion at different speeds and across irregular terrain (*3*–*6*). Muscles that in apes adduct the hallux (such as the m. adductor hallucis and m. fibularis longus), in humans primarily support the pedal arches (*1*, *5*). Permanent plantar arches are a key component of human bipedal walking and running because they contribute to the rigidity of the foot and provide an enhanced mechanical advantage during the propulsive phase of gait (*1*, *7*–*9*). Extant apes, in contrast, exhibit pronounced midtarsal dorsiflexion during heel-off as a result of a mobile midfoot, which permits flexibility for negotiating variably oriented arboreal substrates [(*8*, *9*) and a recent review in (*10*)]. This break is greater in magnitude and is kinematically and anatomically distinct from the medial collapse seen in some humans (*7*, *11*, *12*). Therefore, determining the extent to which the foot of *A. afarensis* had permanent longitudinal and transverse pedal arches is key to deciphering the extent of its commitment to terrestrial bipedality.

Skeletal evidence for the presence of pedal arches in *A. afarensis* has been ambiguous, because key bones from the midfoot have been lacking. The talus (specimens AL 288-1 and AL 333-147) shows a distinct facet for plantar calcaneonavicular (*13*) and cubonavicular ligaments (*9*, *13*, *14*), which are indicative of a human-like medial longitudinal arch. However, unlike in humans, a groove is present for the m. fibularis longus tendon on the plantar surface of the ectocuneiform (AL 333-79) in *A. afarensis*, as seen in apes, perhaps related to the lack of a transverse arch. Dorsal inclination of the tarsal facets has been interpreted to suggest the lack of longitudinal arches in *A. afarensis* (*11*, *12*), and the well-developed navicular tuberosity is argued to be a weight-bearing structure in these hominins (*15*, *16*).

Here we describe AL 333-160, a complete, nearly perfectly preserved fourth metatarsal of *A. afarensis* from Hadar, Ethiopia (Fig. 1). This specimen was recovered from the Hadar locality AL 333 in 2000 during sieving of eroded Denen Dora 2 submember surface deposits of the Hadar Formation. Since 1975, these deposits at the 333 locality have yielded more than 250 hominin fossils that eroded from an in situ horizon dated to ~3.2 million years ago (*17*). We assign AL 333-160 to *A. afarensis*, the only hominin species in an assemblage of >370 hominin specimens so far recovered from the Hadar Formation (*18*). Other partial metatarsals attributed to *A. afarensis* are known from Hadar (*19*), but none is complete enough to address the question

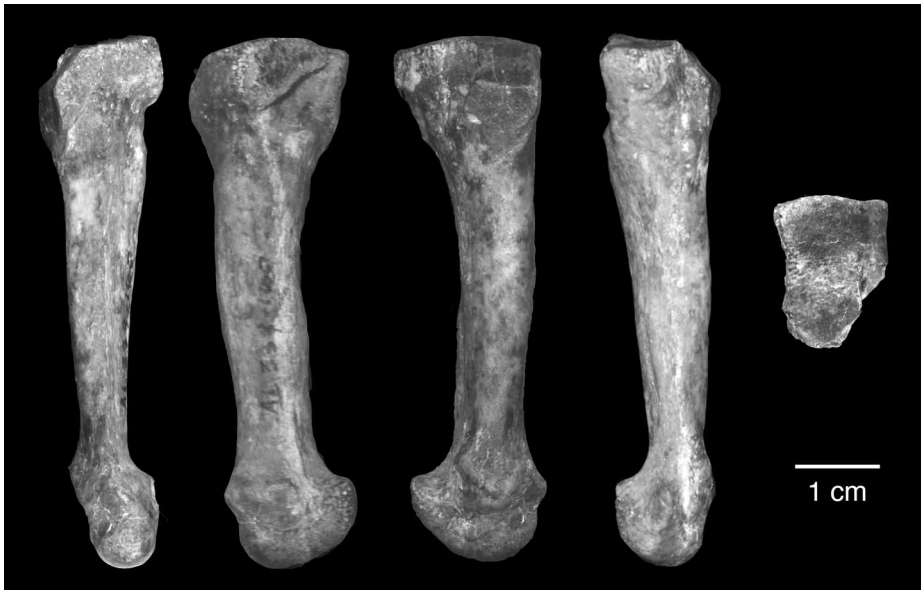

Fig. 1. AL 333-160 left fourth metatarsal in dorsal, lateral, medial, plantar, and proximal views.

[1]Department of Pathology and Anatomical Sciences, M263 Medical Sciences Building, University of Missouri, Columbia, MO 65212, USA. [2]Institute of Human Origins, School of Human Evolution and Social Change, Post Office Box 874101, Arizona State University, Tempe, AZ 85287-4101, USA.

*To whom correspondence should be addressed. E-mail: wardcv@missouri.edu